NANO LETTERS

2007
Vol. 7, No. 6
1474−1479

Nanoscale Analysis of Defect Shedding from Liquid Crystal Interfaces

Benjamin M. Wincure and Alejandro D. Rey*

Department of Chemical Engineering and McGill Institute of Advanced Materials, McGill University, 3610 University Street, Montreal, Quebec H3A 2B2, Canada

Received January 18, 2007; Revised Manuscript Received April 13, 2007

ABSTRACT

A new defect-forming mechanism is predicted for liquid crystals undergoing an isotropic-to-nematic phase transition. A continuum theory characterizes how $+1/2$ defects (D < 30 nm) evolve within and then shed from the interface (cross section ~ 100 nm) of a growing 5CB (4-*n*-4′-pentyl-4-cyanobiphenyl) nanodroplet (20 nm < D < 2000 nm). Free energy density, defect core shapes, and the evolving defect core structure are presented at the nanoscale to better understand liquid crystal anisotropy and orientation during interfacial defect shedding.

Liquid crystals have recently been used in nanotechnologies as templates for nanomaterial fabrication,[1,2] for the assembly of nanoparticles into larger structures with engineered order,[3] to levitate nickel nanowires,[4] to control droplet location and size in nano- and microemulsions,[5] and to control plasmonic response using an arrayed gold nanodot−liquid crystalline composite for better color tuning.[6] In addition, new research is being undertaken to understand the interactions of synthetic liquid crystals and viruses to design materials that incorporate viruses.[7] The distinctive features of liquid crystals arise from their orientational ordering at the nano- and micrometer scale when observed within a temperature range intermediate between the solid and liquid phase (thermotropic liquid crystals) or at particular concentrations within a mixture (lyotropic liquid crystals).[8] Because of this anisotropy, liquid crystalline materials have many important technological applications because they exhibit specific optical, electrical, and mechanical properties[9] and their orientation can be influenced by external fields such as electric[10] or magnetic fields,[11] polarized laser light,[12] shear during processing,[13] and contact with a structured surface or interface.[14]

In many nanotechnologies, a uniform aligned liquid crystal orientation is desired.[1,4,6,15] This is achieved by applying an external force to change the orientation of an already established liquid crystal phase or by aligning the liquid crystal material as the phase forms. To achieve the former, liquid crystals are often put in contact with nanoscale-patterned surfaces or subjected to external fields.[5,6,13,15,16] To achieve alignment during a phase transition, small quantities of single-walled carbon nanotubes have recently been used as seeds for oriented liquid crystal polymer domain growth from the isotropic melt.[17] Homogeneous domains of 10−100 μm on a side were achieved, with the orientation determined by the nanoscale seeds.[17] Alternatively, treated flat surfaces with nanoscale roughness have been used to align a nematic liquid crystal from its isotropic melt.[18−20]

Distorted orientations and the presence of topological defects in liquid crystal orientation also have potential uses for nanoscale devices. For example, emulsions formed from liquid crystals are considered particularly promising candidates for the creation of liquid crystal-based sensors because they have a high surface area, are mobile, and the frustrated distorted states assumed by liquid crystals within droplets provide an additional opportunity to tune the response of liquid crystals to interfacial events.[16] Abbott has shown that liquid crystals can be used to amplify and report the presence of a range of biological species at surfaces according to the degree of distortion and topological defects present when the liquid crystals are in contact with the biological species.[14,18] Distortions and topological defects appear in liquid crystal orientation due to competing external fields, surface anchoring, and/or the geometry of interfaces surrounding the liquid crystal phase.[20] Although many studies have been dedicated to these elastic distortions and defects,[21,22] the purpose of this work is to present the nanoscale events of a newly predicted defect-forming mechanism[23] during an isotropic−nematic liquid crystal phase transition. A continuum theory allows us to magnify the details along a 200 nm length of interface to characterize how a defect core (D < 30 nm) forms and is then deposited into the bulk nematic phase from the advancing isotropic−nematic interface (cross section ~ 100 nm) of a growing thermotropic liquid crystal nanodroplet (20 nm < D < 2000 nm). Investigating this interfacial defect-shedding mechanism is part of the ongoing scientific challenge to understand and control liquid crystal anisotropy and orientation at the nanoscale.

* Corresponding author. E-mail: alejandro.rey@mcgill.ca.

10.1021/nl0701408 CCC: $37.00
Published on Web 05/02/2007

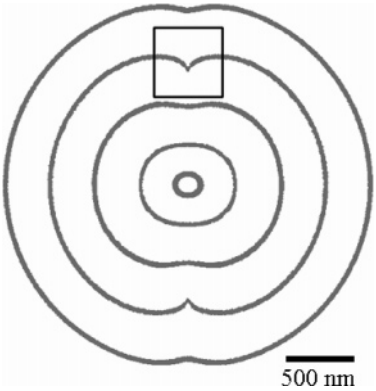

Figure 1. Numerical results for the isotropic−nematic interface of a growing 5CB nanodroplet at 10, 30, 50, 70, and 90 μs after nucleation. $T = 34$ °C. The box identifies where interfacial defect shedding will occur.

For a temperature-driven phase transition of a thermotropic liquid crystal, the nematic phase initially appears in the unstable isotropic phase as nucleating regions with a length scale of 100 nm or less.[24] Nucleated regions that are too small disappear due to their excessively high interfacial energy.[24] However, a nucleated nematic region that is large enough to be stable expands, and its moving isotropic−nematic interface converts more of the isotropic phase into the stable nematic phase.[25] Figure 1 displays numerical results that show the movement of an isotropic−nematic interface at 10, 30, 50, 70, and 90 μs after the nucleation of a circular nematic nanodroplet from the isotropic phase. These numerical results are for the liquid crystal 5CB (4-*n*-4′-pentyl-4-cyanobiphenyl) undergoing an isotropic-to-nematic phase transition at 34 °C, which is below the material's clearing point temperature (34.2 °C). 5CB, a well-studied nematic liquid crystal, is often used to investigate and create new nanotechnologies.[3−5,7,16] During this shallow quench, Figure 1 indicates that the nucleated nanodroplet develops into an ellipsoid (30 μs) and then cusps appear along the isotropic−nematic interface (70 μs). Exactly at these cusps, interfacial defect shedding is expected to occur. The purpose of this letter is to explore, through numerical computations, the details around the interfacial cusp at the nano length scale to characterize the energy, defect core shape, and structure during interfacial defect shedding. The region of interest is shown in Figure 1 enclosed in a 500 nm × 500 nm box.

The kinetics of the isotropic−nematic transition is described using the gradient energy equation:[26]

$$\beta\left(\frac{\partial \mathbf{Q}}{\partial t}\right)_{\boldsymbol{x}} = -\left(\frac{\partial (f_{\mathrm{h}} + f_{\mathrm{g}})}{\partial \mathbf{Q}}\right)^{[\mathrm{s}]} + \left(\nabla\cdot\left(\frac{\partial f_{\mathrm{g}}}{\partial \nabla \mathbf{Q}}\right)\right)^{[\mathrm{s}]} \qquad (1)$$

where the rotational coefficient $\beta = \gamma_1/2Q_{\mathrm{eq}}^2$ is assumed constant and given in terms of the rotational viscosity γ_1 of a uniaxial nematic, $\mathbf{Q}$ is the tensor order parameter that describes the ordering of the liquid crystal material,[9] t is time, [s] identifies that the matrices are symmetric and traceless, and f_{h} and f_{g} are, respectively, the homogeneous and gradient contributions to the free energy density of the system.[9] The free energy density of the isotropic phase, f_{is}, is used as the reference ($f_{\mathrm{is}} = 0$ J/m^3) and therefore does not appear in eq 1. On the basis of the classical Landau−de Gennes continuum theory for nematic liquid crystals,[9,27] the total free energy density f of the system can be expressed in terms of the tensor order parameter $\mathbf{Q}$ and its gradients:

$$f = f_{\mathrm{h}} + f_{\mathrm{g}} + f_{\mathrm{is}} \qquad (2a)$$

$$f_{\mathrm{h}}(\mathbf{Q}) = \frac{a_{\mathrm{o}}(T - T^*)}{2}\mathbf{Q}:\mathbf{Q} - \frac{b}{3}\mathbf{Q}:(\mathbf{Q}\cdot\mathbf{Q}) + \frac{c}{4}(\mathbf{Q}:\mathbf{Q})^2 \qquad (2b)$$

$$f_{\mathrm{g}}(\nabla\mathbf{Q}) = \frac{L_1}{2}\nabla\mathbf{Q}:(\nabla\mathbf{Q})^T + \frac{L_2}{2}(\nabla\cdot\mathbf{Q})\cdot(\nabla\cdot\mathbf{Q}) + \frac{L_3}{2}\mathbf{Q}:(\nabla\mathbf{Q}:(\nabla\mathbf{Q})^T) \qquad (2c)$$

where T is the quench temperature, T^* is the clearing point temperature, i.e., the spinodal temperature below which the isotropic state is unstable,[28] and the experimentally measured material parameters are a_{o}, b, and c (Landau coefficients) and L_1, L_2, L_3 (Landau elastic constants). The following constant material parameters and temperatures were used:[29−33] $a_0 = 0.14 \times 10^6$ J/m^{3}K, $T = 34$ °C, $T^* = 34.2$ °C, $b = 1.8 \times 10^6$ J/m^3, $c = 3.6 \times 10^6$ J/m^3, $L_1 = 3.0 \times 10^{-12}$ J/m, $L_2 = 3.1 \times 10^{-12}$ J/m, $L_3 = 1.5 \times 10^{-12}$ J/m, and $\beta = 0.055$ Ns/m^2. The order in each phase is characterized by the symmetric traceless tensor order parameter:[9]

$$\mathbf{Q} = \mu_n\mathbf{nn} + \mu_m\mathbf{mm} + \mu_l\mathbf{ll}; \qquad \mathbf{Q} = \mathbf{Q}^{\mathrm{T}}; \qquad \mathrm{tr}(\mathbf{Q}) = 0 \qquad (3)$$

where the isotropic state corresponds to zero eigenvalues ($\mu_n = \mu_m = \mu_l = 0$), the nematic uniaxial state to two equal eigenvalues, and the nematic biaxial state to eigenvalues that are different.[34] The orientation is defined by the orthogonal director triad ($\mathbf{n}$, $\mathbf{m}$, $\mathbf{l}$). The uniaxial and biaxial scalar order parameters that measure molecular alignment are, respectively:[35]

$$\mathrm{Q} = (\mathbf{nn}:\mathbf{Q}) = \mu_n \qquad (4)$$

$$\mathrm{P} = (\mathbf{mm} - \mathbf{ll}):\mathbf{Q} = (\mu_m - \mu_l) \qquad (5)$$

The tensor order parameter is initially ($t = 0$) set to:

$$\mathbf{Q}(t=0) = \frac{1}{2}Q_e(T)(3\hat{\delta}_x\hat{\delta}_x - \mathbf{I})(e^{-3.61\times10^{18}(x^2+y^2)}) + \Xi \qquad (6)$$

where Ξ is a symmetric traceless tensor that represents infinitesimal thermal noise, and $Q_{\mathrm{e}}(T)$ is set to 0.184, i.e., the nematic equilibrium scalar order parameter at temperature $T = 34$ °C, the director ($\mathbf{n}$) is initially along the x-axis, and $\mathbf{I}$ is the unit tensor. Neumann boundary conditions ($\partial\mathbf{Q}/\partial x = 0$, $\partial\mathbf{Q}/\partial y = 0$) were applied around the two-dimensional (x,y) computational domain. The finite element method software package COMSOL was used to solve eq 1 using adaptive finite elements and biquadratic basis functions with the direct UMFPACK solver method and a time-dependent

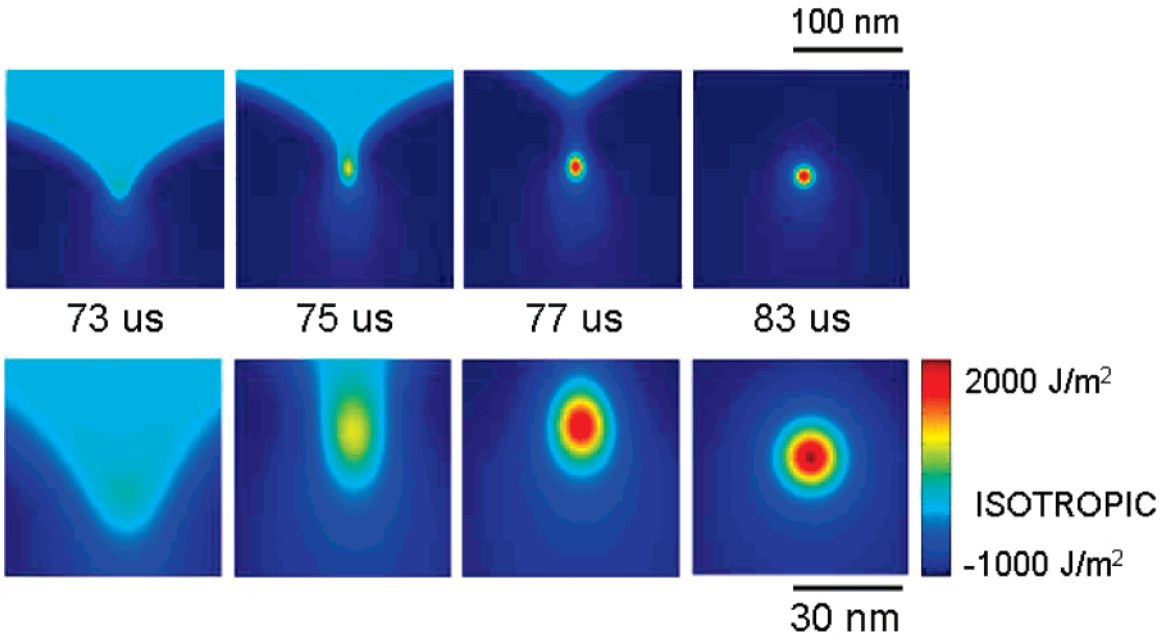

Figure 2. Free energy density during interfacial defect shedding from a cusplike interface at 73−83 μs after nucleation. T = 34 °C. Dark blue = nematic 5CB phase. Red = high free energy density defect region. Top row of figures uses 100 nm scale bar. The magnified figures below use the 30 nm scale bar.

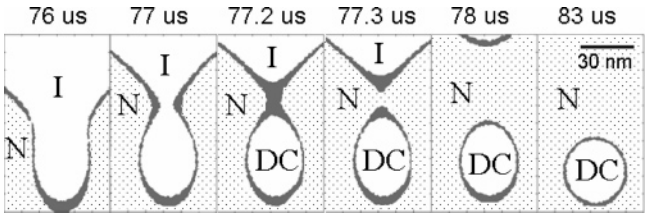

Figure 3. Defect core shape during interfacial defect shedding. I = isotropic phase. N = nematic phase. DC = defect core. Thick gray lines indicate a nematic interface. The isotropic−nematic front moves upward, away from the defect core that is fixed in space.

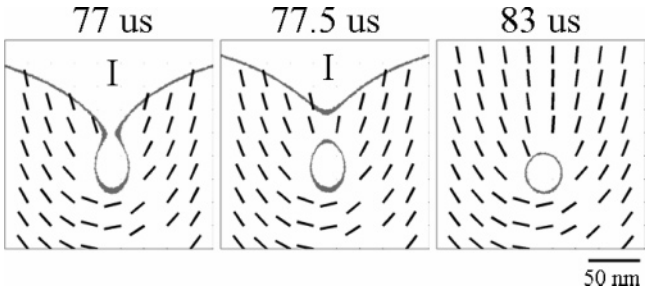

Figure 4. Nematic orientation during interfacial defect shedding. Short black lines indicate the direction of the director **n** in the nematic phase. I = isotropic phase. Thick gray lines indicate a nematic interface. The ellipse and symmetric circle shown surrounded by the nematic phase is the high-energy defect core. The movement of the isotropic−nematic front is upward, away from the defect core that is fixed in space.

backward Euler method. All time steps taken were smaller than 100 ns. Convergence, mesh-independence, and stability were confirmed for each simulation result.

The computed free energy density surrounding the moving isotropic−nematic cusplike interface is shown in Figure 2. At the cusp, a high-energy region forms within the isotropic−nematic interface. This high-energy region is then shed from the interface into the bulk nematic phase within 2 μs as the nanodroplet grows. Within 10 μs, this high energy is concentrated into a symmetric circular space. Defining the border of the nematic interface to have a homogeneous free energy density between −1180 and −1150 J/ m^2, knowing that the computed homogeneous free energy density for the stable nematic phase is very close to −1200 J/m^2, Figure 3 identifies the exact shape relaxation process that occurs as the high-energy region is shed from the isotropic−nematic interface. First, the nematic interface dips down and forms a saclike container, ready to envelope the high-energy region (76 μs). Next, the nematic interface experiences a pinching process, where the top edges of the saclike container are brought together (77 μs). Very quickly after pinching begins, the high-energy region remains attached to the isotropic−nematic interface through just a "thread" of nematic interface (77.2 μs). As the isotropic−nematic interface moves further away, the thread is broken and the nematic phase completely surrounds the high-energy region or defect core (77.3 μs). After the pinching process is completed, this high-energy defect core has an elliptic shape and is surrounded by the nematic phase. Although the isotropic−nematic interface continues to move upward as the nanodroplet grows, the isolated defect core remains fixed in space. Its shape then evolves from an ellipse (major axis = 45 nm, minor axis = 30 nm) to a symmetric circle (D < 30 nm).

Figure 4 shows that, during the pinching process (77 μs), the nematic orientation at the bottom of the cusp is tangential to the nematic interface, but trending toward a homeotropic orientation at the interface further away from the cusp. After pinching, the nematic interface orientation is homeotropic. By 83 μs, the orientation of the nematic phase shown in Figure 4 indicates that interfacial defect shedding has deposited a $+^1/_2$ defect[21] into the bulk nematic phase. The

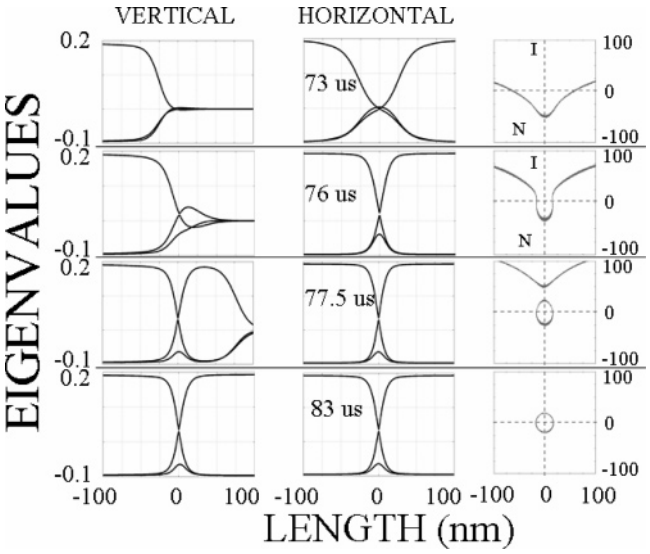

Figure 5. Defect core structure during interfacial defect shedding. At 73 (top row), 76 (second row), 77.5 (third row), and 83 (bottom row) μs, the eigenvalues of the tensor order parameter **Q** are computed to show the structure of the developing defect core. All eigenvalues are between −0.1 and 0.2. The first (second) column presents the eigenvalues calculated along the dotted vertical (horizontal) axes from the third column of figures. The third column figures show the defect core as it sheds from the isotropic−nematic interface, where the defect core region is placed at the center (0,0) of each figure, the thick gray lines indicate a nematic interface, and the *x* and *y* axes are shown in nanometers. *I* = isotropic phase. *N* = nematic phase.

high-energy region shed from the interface is the defect core of this $+1/2$ bulk defect. While the nematic orientation around the $+1/2$ defect is not rotationally symmetric, the shape of the nanoscale defect core is a symmetric circle.

The evolution of the defect core structure is visualized through the eigenvalues of the tensor order parameter, which are calculated in Figure 5 for vertical and horizontal cross sections through the center of the high-energy region that originated at the cusp. This figure shows how a moving isotropic−nematic cusplike interface with a uniaxial structure (73 μs) develops into the complicated structure of a $+1/2$ defect core[21] that contains axial symmetry, biaxiality, and crossing eigenvalues (83 μs). The eigenvalues along the vertical cross section at 73 μs show a simple uniaxial structure for the tensor order parameter across the isotropic−nematic interface at the cusp, i.e., two out of the three eigenvalues are equal and all eigenvalues are gradually reduced to zero as the isotropic phase is approached.[35] As pinching of the interface is about to begin (76 μs), the vertical cross section eigenvalues show that: (i) the nematic phase is uniaxial, i.e., two equal eigenvalues with a scalar order parameter of 0.184, (ii) within the isotropic−nematic interface, biaxiality and crossed eigenvalues develop in the high-energy region that is about to be pinched, and (iii) the largest eigenvalue, i.e., the scalar order parameter, is gradually reduced to zero as the isotropic phase is approached. Once the defect has shed from the interface into the bulk (77.5 μs), the vertical cross section shows that the nematic phase surrounds the defect core and that there is increased biaxiality and eigenvalue crossing within the high-energy defect core. In addition, as a consequence of the defect shedding, the isotropic−nematic interface once again has a simple uniaxial structure. The horizontal cross section eigenvalues illustrate the mirror symmetry of the structure that exists within the high-energy region and the increasing central biaxiality of the developing defect core. At 83 μs, the vertical and horizontal eigenvalues show that the $+1/2$ bulk defect core has a symmetric structure of biaxiality concentrated in a small region at the defect center and crossed eigenvalues. After 76 μs, it is apparent that the horizontal size of the developing defect core structure remains constant. Therefore, when the high-energy region is first isolated from the interface, its minor ellipse axis determines the diameter of the symmetric defect core.

The above results indicate the critical importance of interface shape changes, such as cusp formation, to the defect shedding mechanism. If differential front speeds exist along the interface, then cusps develop where the normal interface velocity is significantly slower at a particular point, i.e., the center of the cusp. An interfacial liquid crystal dynamic shape equation,[36] derived from the Landau−de Gennes model equations, explains in terms of interface stress load, capillary forces, friction (viscous dissipation), and surface viscosity how the normal interface velocity can vary at different points along the interface:

$$\beta_{\perp} w_{\perp} = \underbrace{\mathbf{L}\cdot\mathbf{k}}_{\text{stress load}} + \underbrace{\left(\nabla_s \cdot \mathbf{T}_s\right)\cdot\mathbf{k}}_{\text{capillary forces}} + \underbrace{\beta\, \mathbf{Q}^s : \frac{d\mathbf{Q}^s}{dt}}_{\text{friction}} \qquad (7)$$

where $\beta_{\perp}$ is the surface viscosity, $w_{\perp}$ is the normal interface velocity, $\mathbf{L}\cdot\mathbf{k}$ is the net stress loading at the transverse interface boundaries, ∇_s is the interfacial gradient tensor, $\mathbf{T}_s$ is the interface stress tensor, **k** is the interface unit normal, and $\mathbf{Q}^s$ is the interface tensor order parameter. Previous work[36] has identified that capillary forces ($(\nabla_s\cdot\mathbf{T}_s)\cdot\mathbf{k}$) are responsible for interfacial cusp formation, while the stress load (due to the isotropic−nematic free energy difference (eq 2b)) drives the overall growth of the nanodroplet. Away from where the cusps will develop, capillary forces are negligible ($(\nabla_s\cdot\mathbf{T}_s)\cdot\mathbf{k} \approx 0$). However, where the cusps develop, interface capillary forces increase to significantly oppose the stress load, resulting in a large deceleration of the normal interface velocity. Hence cusp formation is due to deceleration of the front at an interfacial region where the net capillary forces $(\nabla_s\cdot\mathbf{T}_s)\cdot\mathbf{k}$ resist growth; the growth-resisting capillary forces are generated by the orientation gradients in the interfacial region surrounding the cusp. When the defect nucleates and sheds, all terms in eq 7 play a role and the surface viscosity changes transiently so that this part of the moving interface then experiences a fast acceleration followed by a relaxing deceleration. For a detailed analysis, the reader is referred to ref 36.

Considering the above simulation results, interfacial defect shedding can be explained as follows. We assume that a symmetric, aligned nanodroplet is nucleated during a temperature quench where the size of the nucleated region compensates for the high interfacial energy of the droplet.

In the initially aligned nematic nanodroplet, the orientation of the nematic phase along the isotropic−nematic interface is planar (homeotropic) at the top and bottom (left and right) of the droplet and varies incrementally and gradually around the droplet. The droplet grows to replace the higher-energy isotropic phase with a lower-energy nematic phase. However, the velocity of the growing nematic front depends on the orientation of the nematic phase at the isotropic−nematic interface. For a planar anchoring, the interfacial tension is lower and, therefore, as predicted by the Wulff construction,[37,38] the planar-anchored interface moves more slowly so that the droplet adapts an elliptical shape. In addition, as the droplet grows to create more nematic volume, the model predicts that the structure within the nematic−isotropic interface region will also change where appropriate to minimize the free energy of the system. While the homeotropically anchored interface does not undergo any structural changes, the interface structure associated with planar anchoring is modified from a simple uniaxial nematic−isotropic transition to a biaxial transition. Minimization of the system's free energy for the growing nanodroplet occurs due to simultaneous changes in (i) the bulk orientation within the nematic droplet, (ii) the interfacial shape, and (iii) the structure of the isotropic−nematic interface. Cusp formation then takes place where the nematic phase is anchored planar to the interface as capillary forces at this interface region grow to oppose the stress load that drives nanodroplet growth. The result of the differential front speeds, the bulk nematic distortions, and the mixed interface structures is a very high-energy region concentrated at two nematic−isotropic interfacial cusps. Because of their location within the nematic−isotropic interface, these high-energy regions not only have a nematic interface but also an isotropic interface. The defect nucleates as the capillary forces, friction, and surface viscosity all play a role in changing the speed of the complicated planar anchored interface that is surrounded on both sides by a simpler constant velocity uniaxial interface that favors a homeotropic anchoring. At each cusp, a long narrow capillary-shaped high-energy region that opens out to the isotropic phase develops. However, the size of each high-energy region is predetermined by the elasticity of the nematic phase. When its elastically determined maximum size is exceeded, each high-energy region is isolated through a pinching process as its isotropic border is converted to the nematic phase. This is similar to a classical defect formation, i.e., where a large nematic orientation gradient is about to occur, the elasticity of the material determines whether nematic molecular ordering is still possible or if, instead, the molecular ordering must change to reduce the elastic energy in this region. When the orientation gradient is too large, it is impossible for the nematic phase to maintain a continuous phase and instead the system nucleates a region of non-nematic molecular ordering. Although this defect core of non-nematic molecular ordering has a relatively high-energy density, its energy density is still less than that of a nematic phase with a large orientation gradient. The pinching process to isolate a high-energy nanometer-size region is reminiscent of similar processes at the micrometer scale, for example, the formation of a micrometer-sized water droplet from a slow dripping capillary.[39] In both situations, isolation or breakaway of a region occurs when the size of that region becomes unstable upon the addition of a further increment of material to the region. However, it is clear that the forces that cause capillary pinching and phase isolation at micrometer vs nano length scales for these two examples occur for very different reasons. In the formation of micrometer water droplets, new material is added only to the breakaway phase and a balance of surface tension and an external force, i.e., gravity, determines the unstable droplet size.[39] In interfacial defect shedding, material elasticity and an ongoing isotropic-to-nematic phase transition are responsible for nanoscale pinching, where during the phase transition, material is added to both the phase to be isolated and the surrounding pinching phase. The elasticity forces, which are characteristic of liquid crystals but not regular isotropic liquids such as water, determine when a high-energy region becomes too large and, therefore, isolation or breakaway is initiated.

Finally, we would like to comment on the connection between the simulation predictions and current experiments. To our knowledge, there are no available experimental methods to investigate the nanoscale details of nematic textures and defects in growing nematic 5CB nanodroplets surrounded by their own isotropic phase. Experimental observation of interfacial defect shedding that produces two $+1/2$ defects in growing nanodroplets is nontrivial given the fast time and small length scales involved. Although optical methods are commonly used to study growing liquid crystal droplets,[40−41] the resolution of these techniques is limited to the micrometer length scale.[42] In contrast, the deuterium nuclear magnetic resonance (^{2}H NMR) technique has been used successfully in confined submicrometer geometries.[42−44] Experimental observations of nematic 5CB in cylindrical cavities ($R < 400$ nm) of Nucleopore membranes surface-treated with lecithin have identified an equilibrium planar−polar nematic texture that is very similar to the (nonequilibrium) nematic texture predicted to occur immediately before interfacial defect shedding.[42] Lecithin as a surface treatment in these cavities weakens the anchoring interaction between 5CB and the confining surface while still favoring homeotropic anchoring. The confinement radius and interfacial anchoring of the Nucleopore lecithin experiments are similar to those predicted here for a growing nematic nanodroplet just before interfacial defect shedding, so this experimental result is an important contribution toward model validation. Finally, it is understood that experimental results, whether they be from optical methods or more sensitive ^{2}H NMR techniques, will always be interpreted based on an expectation of what the nematic texture might be. For example, for confined nematic structures, the characteristic features of ^{2}H NMR line shapes are the width and shape of the spectral patterns.[42] For a spectral pattern that has not been seen before, predicted nematic textures are required in order to create a simulated spectral pattern that is then carefully compared to the newly observed experimental ^{2}H NMR spectrum.[42] This process is crucial to interpret experimental

results. We therefore expect that detailed simulation predictions for liquid crystals in nanoscale nonequilibrium conditions will play a critical role in interpreting results from new future experimental techniques that will be developed for liquid crystals in nanotechnology.

In conclusion, the numerical computations presented here give details at the nano length scale about a newly predicted mechanism for defect creation in soft matter liquid crystal materials. This mechanism, called "interfacial defect shedding",[23] occurs during an isotropic-to-nematic phase transition and predicts that $+1/2$ bulk nematic defects are generated from the moving isotropic−nematic interface of an isolated growing 2-D liquid crystal nanodroplet (20 nm < D < 2000 nm). By computationally focusing on a 200 nm length of interface, we have calculated the free energy relaxation and the shapes and ordering associated with the phase transition to explain how the complicated structure of a $+1/2$ bulk nematic defect core[21] that contains axial symmetry, biaxiality, and crossing eigenvalues can evolve from a high-energy region within the advancing isotropic−nematic interface. These new results contribute to the emerging nanophysics of liquid crystals, where it is clear that understanding and/or controlling the defects, distorted and uniform orientations of this soft matter phase will dictate its potential as functional materials for nanoscale applications.

Acknowledgment. This work was supported by a grant from the Natural Science and Engineering Research Council of Canada. B.W. is grateful for financial support from the Robert G. H. Lee Fellowship program at McGill University.

References

(1) Andersson, M.; Alfredsson, V.; Kjellin, P.; Palmqvist, A. E. C. *Nano Lett.* **2002**, *2*, 1403−1407.
(2) Lee, S.-W.; Mao, C.; Flynn, C. E.; Belcher, A. M. *Science* **2002**, *296*, 892−895.
(3) Lynch, M. D.; Patrick, D. L. *Nano Lett.* **2002**, *2*, 1197−1201.
(4) Lapointe, C.; Hultgren, A.; Silevitch, D. M.; Felton, E. J.; Reich, D. H.; Leheny, R. L. *Science* **2004**, *303*, 652−655.
(5) Poulin, P.; Weitz, D. A. *Phys. Rev. E* **1998**, *57*, 626−637.
(6) Kossyrev, P. A.; Yin, A.; Cloutier, S. G.; Cardimona, D. A.; Huang, D.; Alsing, P. M.; Xu, J. M. *Nano Lett.* **2005**, *5*, 1978−1981.
(7) Jang, C.-H.; Cheng, L.-L.; Olsen, C. W.; Abbott, N. L. *Nano Lett.* **2006**, *6*, 1053−1058.
(8) Collings, P. J. *Liquid Crystals: Nature's Delicate Phase of Matter;* Princeton University Press: Princeton, NJ, 2002; pp 16.
(9) de Gennes, P. G.; Prost, J. *The Physics of Liquid Crystals*, 2nd ed.; Clarendon Press: New York, 1993; pp 41−97.
(10) Korner, H.; Shiota, A.; Bunning, T. J.; Ober, C. K. *Science* **1996**, *272*, 252−255.
(11) Lee, S.-W.; Mao, C.; Flynn, C. E.; Belcher, A. M. *Science* **2002**, *296*,892−895.
(12) Gibbons, W. M.; Shannon, P. J.; Sun, S. T.; Swetlin, B. J. *Nature* **1991**, *351*, 49−50.
(13) Zakharov, A. V.; Dong, R. Y. *Phys. Rev. E* **2002**, *65*, 052701.
(14) Gupta, V. K.; Skaife, J. J.; Dubrovsky, T. B.; Abbott, N. L. *Science* **1998**, *279*, 2077−2080.
(15) Lynch, M. D.; Patrick, D. L. *Nano Lett.* **2002**, *2*, 1197−1201.
(16) Tjipto, E.; Cadwell, K. D.; Quinn, J. F.; Johnston, A. P. R.; Abbott, N. L.; Caruso, F. *Nano Lett.* **2006**, *6*, 2243−2248.
(17) Mrozek, R. A.; Kim, B.; Holmberg, V. C.; Taton, T. A. *Nano Lett.* **2003**, *3*, 1665−1669.
(18) Luk, Y.-Y.; Tingey, M. L.; Hall, D. J.; Israel, B. A.; Murphy, C. J.; Bertics, P. J.; Abbott, N. L. *Langmuir* **2003**, *19*, 1671−1680.
(19) Brake, J. M.; Daschner, M. K.; Luk, Y. Y.; Abbott, N. L. *Science* **2003**, *302*, 2094−2097.
(20) Frank, F. C. *Discuss. Faraday Soc.* **1958**, *25*, 19−28.
(21) Sonnet, A.; Kilian, A.; Hess, S. *Phys. Rev. E* **1995**, *52*, 718−722.
(22) Gupta, G.; Rey, A. D. *Phys. Rev. Lett.* **2005**, *95*, 127802.
(23) Wincure, B.; Rey, A. D. *J. Chem. Phys.* **2006**, *124*, 244902; *Virtual J. Nanoscale Sci. Technol.* **2006**, *14*, 115.
(24) Lavrentovich, O. D. In *Patterns of Symmetry Breaking*; Arodz, H., Dziarmaga, J., Zurek, W. H., Eds.; NATO Science Series II: Mathematics, Physics and Chemistry; Kluwer Academic Publishers; New York, 2003; Vol. 127, pp 161−195.
(25) Bronnikov, S.; Dierking, I. *Phys. Chem. Chem. Phys.* **2004**, *6*, 1745−1749.
(26) Popa-Nita, V.; Sluckin, T. J.; Wheeler, A. A. *J. Phys. II* **1997**, *7*, 1225−1243.
(27) Schiele, K.; Trimper, S. *Phys. Status Solidi. B* **1983**, *118*, 267−274.
(28) Yokoyama, H. In *Handbook of Liquid Crystal Research*; Collins, P. J., Patel, J. S., Eds.; Oxford University Press, New York, 1997; pp 179−235.
(29) Coles, H. J. *Mol. Cryst. Liq. Cryst.* 1978, *49*, 67−74.
(30) Bogi, A.; Faetti, S. *Liq. Cryst.* **2001**, *28*, 729−739.
(31) *Physical Properties of Liquid Crystals*: *Nematics*; Dunmur, D. A., Fukuda, A., Luckhurst, G. R., Eds.; INSPEC, The Institute of Electrical Engineers: London, 2001; pp 97, 220.
(32) Leslie, F. M. *Continuum Mech. Thermodyn.* **1992**, *4*, 167−175.
(33) Skarp, K.; Lagewall, S.; Stebler, B. *Mol. Cryst. Liq. Cryst.* **1980**, *60*, 215−236.
(34) Rey, A. D. *Macromol. Theory Simul.* **1995**, *4*, 857−872.
(35) de Gennes, P. G. *Mol. Cryst. Liq. Cryst.* **1971**, *12*, 193−214.
(36) Wincure, B.; Rey, A. D. *Continuum Mech. Thermodyn.* **2007**, http://dx.doi.org/10.1007/s00161-007-0043-z.
(37) Emmerich, H. *The Diffuse Interface Approach in Materials Science*; Springer-Verlag: New York, 2003.
(38) Virga, E. G. *Variational Theories for Liquid Crystals*; Chapman and Hall: London, 1994.
(39) Middleman, S. *Modeling Axisymmetric Flows: Dynamics of Films, Jets, and Drops*; Academic Press: New York, 1995; pp 94−97.
(40) Bronnikov, S.; Dierking, I. *Physica B* **2005**, *358*, 339−347.
(41) Bronnikov, S.; Dierking, I. *Phys. Chem. Chem. Phys*. **2004**, *6*, 1745−1749.
(42) Crawford, G. P.; Allender, D. W.; Doane, J. W. *Phys. Rev. A* **1992**, *45*, 8693−8708.
(43) Crawford, G. P.; Vilfan, M.; Doane, J. W. *Phys. Rev. A* **1991**, *43*, 835−842.
(44) Erdmann, J. H.; Zumer, S.; Doane, J. W. *Phys. Rev. Lett*. **1990**, *64*, 1907−1910.

NL0701408